Investigation of Graphite Nozzle Erosion in Hybrid Rockets Using O2/HDPE

Landon Kamps[1], Shota Hirai[2], Kazuhito Sakurai[3], Tor Viscor[4],
Hokkaido University, Sapporo, 060-8628, Japan

Yuji Saito[5],
Touhoku University, Sendai, 980-8579, Japan

Raymond Guan[6],
University of Toronto, Toronto, M5S 3G3, Canada

Hikaru Isochi[7], Naoto Adachi[8],
Uematsu Electric Co., Ltd., Akabira, 079-1101, Japan

Mitsunori Itoh[9],
IHI Corporation, Yokohama, 235-8501, Japan

and

Harunori Nagata[10]
Hokkaido University, Sapporo, 060-8628, Japan

A recently developed reconstruction technique is used to investigate graphite nozzle erosion in two scales of hybrid rocket motors, 30N-thrust class and 2000N-thrust class, using oxygen as the oxidizer and high-density polyethylene as the fuel. Thermocouple measurements taken from within the nozzles are used to estimate nozzle throat wall temperature. Forty-four static firing tests were conducted under varying experimental conditions to confirm the validity of the reconstruction technique results, investigate the conditions at the onset of erosion and to formulate an empirical predictive model of nozzle erosion rate. Results show that a single formula that treats the combustion gas as a single oxidizing agent for which heterogenous rate constants are functions of equivalence ratio can satisfactorily replicate the

[1] Project researcher, Faculty of Engineering, Department of Mechanical and Space Engineering, Member AIAA.
[2] Master's course student, Department of Mechanical and Space Engineering.
[3] Master's course student, Department of Mechanical and Space Engineering.
[4] Doctor's course student, Department of Mechanical and Space Engineering, Member AIAA.
[5] Assistant professor, Faculty of Engineering, Department of Aerospace Engineering, AIAA Member.
[6] Master's course student, Department of Mechanical and Industrial Engineering, AIAA Member.
[7] Lead engineer, Research and Development.
[8] Engineering technician, Research and Development.
[9] Project researcher, Heat & Fluid Dynamics Department.
[10] Professor, Faculty of Engineering, Department of Mechanical and Space Engineering, Member AIAA.

erosion rate of graphite by a combustion gas containing multiple oxidizing species. Furthermore, the chemical-kinetic limited conditions of the onset of nozzle erosion are specified by a novel empirical correlation which shows that erosion begins at lower temperature and pressure in oxidizer rich combustion gas than in fuel rich combustion gas.

Nomenclature

A,b,E	=	Arrhenius equation constants
a,b,c,d	=	placeholders in Eq. (12)
c_p	=	constant pressure specific heat, J/kg-K
c^*	=	characteristic exhaust velocity, m/s
d	=	diameter, m
D	=	(mass) diffusion coefficient, m^2/s
F	=	thrust, N
k	=	thermal conductivity, W/m-K or heterogenous rate constant
M	=	mass remaining, kg
$\dot{m}$	=	mass flow/consumption rate, kg/s
P	=	pressure, Pa
R_u	=	universal gas constant, J/kmol-K
r	=	radial position from nozzle centerline, m
Δr	=	radial node spacing in the nozzle mesh, m
$\dot{r}$	=	(nozzle) erosion rate, m/s
Re	=	Reynolds number
Sc	=	Schmidt number
T	=	Temperature, K
t	=	(firing) time, s
Δt	=	time step, s
U	=	uncertainty
$\beta_1, \beta_2, \beta_3$	=	empirical constants in Eq. (5)

α	=	thermal diffusivity, m^2/s
γ	=	specific heat ratio
η^*	=	characteristic exhaust velocity efficiency
λ	=	thrust correction factor
ξ	=	oxidizer-to-fuel-mass ratio
ρ	=	density, kg/m^3
Φ	=	equivalence ratio
Ψ,ψ	=	calculation residual terms
$\bar{}$	=	overbar, to indicate a time-averaged value

Subscripts

a	=	atmospheric
b	=	(burn) time
c	=	chamber position
calc,meas	=	distinguishes a calculated value or a measured value
e	=	nozzle exit plane position
f	=	final
fu	=	fuel
i	=	oxidizing species index in Eq. (1) or radial node index in Eq. (12)
j	=	reaction index in Eq. (2) or time index in Eq. (12)
n	=	nozzle
n1,n2,n3	=	thermocouple positions within the nozzle
o	=	initial
on	=	(time) at the onset of erosion
ox	=	oxidizer
t	=	nozzle throat position
w	=	nozzle wall

Acronyms

CEA	=	Chemical Equilibrium with Applications
GFRP	=	Glass-Fiber Reinforced Plastic
HDPE	=	High Density Polyethylene
NTRT	=	Nozzle Throat Reconstruction Technique
TTRT	=	Throat Temperature Reconstruction Technique

I. Introduction

THE theory of carbon-based chemical rocket nozzle erosion is relatively well understood. A collection of papers from the 1960s satisfactorily explain nozzle erosion as the heterogenous (oxidation) reaction of the surface of a nozzle with constituents of the combustion gas (see Refs. [1-3]). Nozzle erosion continues in time so long as the rate of supply of reactant gas to the surface is matched by the heterogeneous reaction rate of the nozzle material, where the supply of gas is driven by the concentration gradients of reacting species within the boundary layer. In practice, there is still much room for improvement towards predicting the rate of nozzle erosion, either empirically or through computational methods.

There is essentially one large obstacle that has remained in the way of the empirical analysis of nozzle erosion, the large amount of data necessary to make statistically meaningful correlations. The nondimensional formula of Ref. [3] offers some insight into what non-dimensional parameters can be expected to govern such correlations, but the eight exponents and one constant of this formula were determined using only 43 data. The same can be said for the contributions of Keswani et al. (4 exponents and 1 constant from 27 data) [4], and Evans (1 exponent and 3 constants from 19 data) [5]. Evans' work is noteworthy in that it elucidates the phases of erosion through the presentation of time-resolved erosion histories. In tests where nozzle erosion occurred, it is seen to begin at some conspicuous time seconds after ignition and proceed at a slightly decreasing rate. Due to the availability of time-resolved histories of erosion, it was possible for Evans to back out multiple data from each test, however, the time-averaged analysis proved to be sufficient for the correlation of erosion rate data within the study and the analysis concluded in this way. Furthermore, nozzle wall temperature measurements were not included in these empirical formulations. Due to the lack of data, and in particular the lack of nozzle wall temperature data, the applicable range of past empirical correlations is unclear.

The authors of this paper, who are developing hybrid rocket motors, foresaw some potential shortcomings of these results in the context of hybrid rocket development. First, the formulas from previous research do not include all

abundant oxidizing gas species of hybrid rocket combustion gas, predominately CO_2, H_2O, O, OH and O_2. For example, Kiwanis et al's formula only considers the mole fractions of CO_2 and H_2O, and Evan's formula only considers the mass fraction of OH and H_2O. Furthermore, Evans weights the mass fraction of H_2O at 6% that of OH, but it is not clear if this weight remains valid when other species are included in the formula. Second, neither formula considers the effect of nozzle wall temperature. Wall temperature is crucial for understanding the (chemical) reactivity of the nozzle, and may also affect the mass diffusivity of gas species within the concentration boundary layer due to the close proximity to the nozzle surface.

When focusing on the erosion of solid rocket nozzles, the treatment of nozzle erosion as a predominantly diffusion-limited process may be acceptable, particularly when the initial nozzle thermal transient is relatively short compared to the overall firing duration. In the case where the subject of nozzle erosion is a hybrid rocket motor, this convention no longer stands. Hybrid rockets can be shut down and restarted multiple times during the course of a firing as in experiments by Whitmore et al. [6] and Jens et al. [7], and regenerative cooling is feasible as shown by the experiments of Yasua et al. [8], meaning that a much larger portion of firing may take place in the chemical-kinetic limited regime of erosion. Data from a larger set of gas compositions, and data of nozzle wall temperature are essential for a full understanding of nozzle erosion, particularly in the context of hybrid rocket motor development.

This study aims to make a lasting contribution to the field of nozzle erosion by overcoming the shortcomings of previous studies. This will be done by building upon the correlations of previous researchers to include the effect of nozzle wall temperature, and improve the reliability and applicability of correlations by ensuring an adequate number of data are collected with respect to the number of fitting constants. The experimental methods of Ref. [9] and [10] are employed to determine the histories of nozzle erosion in a cost-effective way using hybrid rocket motors as a data collection apparatus. This method only requires measurement histories of oxidizer flow rate, pressure and thrust, and endpoint (i.e. pre- and post-firing) measurements of mass and nozzle throat diameter. This means that it can equally be applied to multiple scales of tests with the same measurement equipment. Since hybrid rocket motors are used for data acquisition, the equivalence ratio of combustion gas changes in time, broadening the domain of data that can be collected from a single test. Additionally, a new technique is introduced to determine time-resolved nozzle wall temperature based on two temperature measurement histories taken from within the body of the nozzle close to the nozzle throat and the one-dimensional heat equation in cylindrical coordinates.

II. Method

The concept of this study is to experimentally investigate graphite nozzle erosion in hybrid rockets by conducting controlled and repeatable static firing tests on two scales of hybrid rocket motors: 30N-thrust class and 2000N-thrust class; and analyzing the data with the help of the data reduction methods previously introduced in Refs. [9] and [10]. The formula proposed for empirical correlation is a modification of the Arrhenius equation to include the effect of combustion gas composition and turbulent gas diffusion. The uncertainty of experimental measurements which propagate through the data reduction methods is accounted for through sensitivity analysis. The governing equations and assumptions of the estimation of nozzle wall temperature histories using thermocouple measurements from within the nozzle, referred to as the "Throat Temperature Reconstruction Technique (TTRT)," will be discussed in detail.

A. Empirical Model

An empirical formula based on the Arrhenius equation will be proposed in this section. It is widely accepted that nozzle erosion is the result of heterogenous chemical reactions between the nozzle surface and the combustion gas passing over it, predominately CO_2, H_2O, O, O_2 and OH [1-3,11-13]. Thus, the erosion rate at the nozzle surface $\dot{r}$ can be calculated by Eq. (1):

$$\dot{r} = \sum \dot{r}_i \qquad i: \text{ oxidizing species} \tag{1}$$

where $\dot{r}_i$ is the contribution to erosion rate from the *i*-th oxidizing species. In general, the erosion contribution of each oxidizing species may be calculated according to an Arrhenius equation of the form in Eq. (2):

$$\rho_n \dot{r}_i = k_j p_i^{n_j} = A_j T_w^{b_j} \exp\left(\frac{-E_j}{R_u T_w}\right) p_i^{n_j} \qquad j: \text{ chemical reaction} \tag{2}$$

Here, k_j and n_j are the heterogenous rate constant and pressure exponent of the *j*-th chemical reaction, p_i is the partial pressure of species *i* at the nozzle wall, and ρ_n is the nozzle density. The terms A_j, b_j, and E_j are empirical constants, and R_u is the universal gas constant.The histories of equivalence ratio Φ, nozzle (throat) erosion rate $\dot{r}$, and nozzle (throat) wall temperature T_w can be determined using data reduction techniques, but the partial pressures of the

oxidizing species p_i are not readily available. To capture the emergent properties of erosion rate that result from the interaction of each separate oxidizing species, the measurable value of Φ will be used. It is fruitful to analyze the trend in erosion rates according to Eqs. (1) and (2) by making the approximation that p_i is proportional one-to-one to the mole fractions of oxidizing species X_i. The resulting functional dependency of erosion rate on equivalence ratio is depicted in Fig. 1, where the erosion rate contributions of the five most abundant oxidizing species – CO_2, H_2O, O, O_2, and OH – are designated by the black lines with markers, and the sum of these contributions is depicted by the black line without markers. In this analysis, the pressure and wall temperature were set at 1 MPa and 3000 K, respectively. The mole fractions of oxidizing species were calculated using NASA Chemical Equilibrium with Applications (CEA) [14], and the empirical constants of Chelliah et al. [15] were used for Arrhenius equation calculations. The magnitudes of erosion rates are exaggerated because gas diffusion is neglected. The key takeaway from this analysis is that the shape of the total erosion rate curve is similar to that of a skewed distribution, with a peak in slightly oxidizer rich conditions. This dependency on Φ was also predicted by Bianchi and Nasuti in Ref. [13], and appears in the experimental results of Ref. [9].

In this section, an empirical model for erosion rate is developed based on the Arrhenius equation and the trends observed in Fig. 1. The concept of this empirical model is to represent the behavior of the sum of contributions of all oxidizing species to nozzle erosion through a single equation. The term "bulk" combustion gas is used in the following sections to represent the fluid that exhibits the erosive behavior of the combustion gas mixture passing through the nozzle. The partial pressure terms p_i in Eq. (2) are considered to be dependent on the total pressure P in Pa, scaled by the diffusion mass flux term of Eq. (3):

$$\left(\frac{\rho D_{\mathrm{CO}}}{\delta_{\mathrm{CO}}}\right)_w \propto \frac{\rho_w D_{\mathrm{CO},w}}{d\,\mathrm{Re}^{-0.83}\,\mathrm{Sc}_{\mathrm{CO}}^{-0.44}} \tag{3}$$

Here the subscript w means that the value under consideration is calculated based on the nozzle wall temperature. The term ρ_w [kg/m^3] is the density of combustion gas mixture at the nozzle wall temperature, which is scaled down from bulk fluid temperature in the chamber according to the perfect gas law. The term $D_{\mathrm{CO},w}$ [m^2/s] is the binary diffusion coefficient of the product gas (carbon monoxide) in air at the nozzle wall temperature. These values are calculated according the Champman-Enskog equations and values as presented in Ref. [16] (p. 708). The formula for the

concentration boundary layer thickness of carbon monoxide δ_{CO} [m] is taken from the results of Gilliland and Sherwood [17]. In this formula, the Schmidt number of carbon monoxide Sc_{CO} is calculated using the molecular weight of the combustion gas *MW* instead of the mass density according to Eq. (4):

$$Sc_{CO} = \frac{\mu}{MWD_{CO,w}} \tag{4}$$

The reaction-diffusion process underlying nozzle erosion can now be captured by a single empirical formula which non-dimensionalizes the erosion mass flux using the diffusion term of Eq. (4), and treats the Arrhenius constants as a distribution-type function of equivalence ratio:

$$\frac{d\dot{r}}{D_{CO,w}} = \beta_1 \Phi^{\beta_2} \exp(-\beta_3 \Phi) T_w^b \exp\left(-\frac{E}{T_w}\right) P^n \left(\frac{\rho_w}{\rho_n}\right) \mathrm{Re}^{0.83} \mathrm{Sc}_{CO}^{0.44} \tag{5}$$

Here, β_1, β_2 and β_3 are empirical constants of the equivalence ratio dependency. The Arrhenius empirical constants *b*, *n*, and *E* in Eq. (5) are no longer listed with subscript *j*, to distinguish them as representative of the entire spectrum of reactions taking place between the nozzle wall and the bulk combustion gas rather than a specific reaction. Thus, there are six empirical constants that will be determined through correlation of experimental data. As a simple approximation for the number of data required for a statistically significant correlation, we can assume: 9 data (β_1, β_2 and β_3) x 6 data (*b* and *E*) x 3 data (*n*) > 160 data. One downside to the formula in Eq. (5) is that the constant β_1 must carry units of $K^{-b}Pa^{-n}$. This type of unit dependency can complicate the determination of empirical constants through the method of least squares.

B. The Nozzle Throat Reconstruction Techniques

The ballistic reconstruction techniques referred as the Nozzle Throat Reconstruction Technique (NTRT) and NTRT$^+$ were the main topics of study in Refs. [9] and [10], respectively. The underlying algorithms of these techniques will be only briefly introduced here. The key assumptions underlying the NTRT calculations are the thrust correction factor λ, and/or theoretical characteristic exhaust velocity c_{th}^* efficiency η^* are constant during a firing, and that combustion gas passing through the nozzle is adiabatic and chemically frozen. By making these assumptions, it

becomes possible to determine the (wetted) nozzle throat diameter d_t and oxidizer-to-fuel-mass ratio ξ histories from readily available static firing test data and NASA CEA. The algorithms underlying the NTRT/NTRT$^+$ calculations are the minimization of the residual terms Ψ_{NTRT} defined by Eq. (6):

$$\Psi_{NTRT} = \begin{cases} \sqrt{\left(1-\frac{\sum \dot{m}_{fu}\Delta t}{\Delta M_{fu}}\right)^2 + \left(1-\frac{d_t(t_b)}{d_{t,f}}\right)^2} = f(\lambda,\eta^*) & \text{for the NTRT} \\ \sqrt{\left(1-\frac{d_t(t_b)}{d_{t,f}}\right)^2} = f(\lambda) & \text{for the NTRT}^+ \end{cases} \tag{6}$$

Here the term $d_t(t)$ is the calculated history of nozzle throat diameter such that $d_t(t_b)$ represents the calculated value for final nozzle throat diameter, i.e. the value at the burn time t_b. The term ΔM_{fu} is the measured overall fuel mass consumption, and the term $\Sigma\dot{m}_{fu}$ is the calculated value. The NTRT residual term Ψ_{NTRT} represents the discrepancy observed between overall fuel mass consumption and the nozzle throat diameter as measured pre-/post-firing and the corresponding results of theoretical calculations when assuming some value for η^* and λ. The *f*-terms on the right-hand side of Eq. (6) are used to explain the functional dependency of the residual term and do not represent any specific functions. To solve the system of equations of the NTRT, the authors currently use a two-variable Newton-Raphson iteration to simultaneously solve for η^* and λ together, which typically converges within four iterations. The values of d and ξ or η^* are determined through separate iterative procedures that takes place at every time t. These iterative procedures are to reduce the residual terms ψ_F defined by Eq. (7):

$$\psi_F(t) = \left|1-\frac{\lambda\eta^*\dot{m}(t)u_e(t)+\left(P_e(t)-P_a\right)A_e}{F(t)}\right| = \begin{cases} f(\xi(t)) & \text{for the NTRT} \\ f(\eta^*(t)) & \text{for the NTRT}^+ \end{cases} \tag{7}$$

where u_e, P_e, P_a, and A_e are the theoretical nozzle exit velocity in m/s, theoretical nozzle exit pressure in Pa, atmospheric pressure in Pa, and nozzle exit cross-sectional area in m^2, respectively. As in Eq. (6), the *f*-terms on the right-hand side Eq. (7) were added to explain the functional dependency of the residual. In many cases, using open iterative procedures such as the Newton-Raphson method to solve for ξ leads to issues with convergence, and for this reason it is recommended that a hybrid of an open and closed iterative procedure be employed – Newton-Raphson and

Bi-section, for example. The values of u_e and P_e are solved for with the assistance of NASA CEA. The nozzle throat diameter d_t [m] is calculated explicitly by rearranging the c^* equation, Eq. (8):

$$d_t = \sqrt{\frac{4}{\pi}\frac{\eta^* c_{th}^* \dot{m}_{ox}\left(1+1/\xi\right)}{P_c}} \tag{8}$$

The NTRT$^+$ is required for firing tests that burn in fuel rich conditions ($\Phi > 1.7$) for a majority of the firing duration, because a region of multiple ξ solutions exist for the set of Eqs. (7) and (8). The NTRT$^+$ is completed by repeating tests with the combustion time as the independent variable to back out the time-resolved value for ξ, and using this as input data to Eqs. (7) and (8). The additional input history allows for the η^* to be solved at every time step, rather than be treated as a constant. The downside of the NTRT$^+$ is that multiple tests must be conducted before any analysis can be done, and experimental uncertainty may be introduced by non-repeatable aspects of a set of tests.

C. Throat-Temperature Reconstruction Technique

Nozzle wall temperature is an important factor in evaluating nozzle throat erosion because it directly relates to the reactivity of the nozzle surface with oxidizing species in the combustion gas. The method to estimate nozzle wall temperature in this study is founded on temperature measurements taken within the nozzle during static firing tests, and the conduction of heat within the nozzle. The key assumptions underlying TTRT calculations are that heat transfer at the nozzle throat is one-dimensional in the radial direction, and that internal heat generation is negligible. By making these assumptions, it is possible to determine the T_w history using thermocouple measurements from within the nozzle throat. The algorithm underlying the TTRT calculations is the minimization of the residual term Ψ_{TTRT} defined by Eq. (9):

$$\Psi_{TTRT}\left(t\right) = 1 - \frac{T_{n1,calc}(t)}{T_{n1,meas}(t)} = f\left(T_w\right) \tag{9}$$

Here, $T_{n1,calc}$ and $T_{n1,meas}$ are the calculated and measured temperatures at the position of the thermocouple placed closest to the nozzle throat in K. The nozzle wall temperature is iterated to minimize the discrepancy between these

values at every time step. The heat conduction equation is employed to determine $T_{n1,calc}$ along with the temperature profile between T_w and a second thermocouple measurement taken further from the throat than T_{n1}, referred to as T_{n2}.

In general, the governing differential equation for 1D conductive heat flux in cylindrical coordinates reduces to Eq. (10) by assuming negligibly small axial and circumferential temperature gradients, no internal heat generation, and constant thermal diffusivity:

$$\frac{\partial T}{\partial t} = \frac{\alpha}{r}\frac{\partial}{\partial r}\left(r\frac{\partial T}{\partial r}\right) \tag{10}$$

Here, α is the thermal diffusivity of the nozzle in m^2/s, T is the local instantaneous temperature in K, and r is the radial position from the centerline of the nozzle in m. Approximating the partial derivatives in Eq. (10) by the first term of the Taylor series expansions near the points of interest, consolidating terms, and rearranging yields the finite difference equation shown by Eq. (11):

$$\begin{gathered} a_i^j T_{i-1}^{j+1} + b_i^j T_i^{j+1} + c_i^j T_{i+1}^{j+1} + d_i^j T_i^j = 0 \\ a_i^j = 2\alpha^j r_i \Delta t - \alpha^j \Delta r \Delta t \\ b_i^i = -(4\alpha^j r_i \Delta t + 2r_i \Delta r^2) \\ c_i^j = \alpha^j \Delta r \Delta t + 2\alpha^j r_i \Delta t \\ d_i = 2r_i \Delta r^2 \end{gathered} \tag{11}$$

where Δt is a time step set to accommodate the response time of thermocouples in s, Δr is the radial mesh spacing, subscript i specifies the radial node index, and superscript j represents the time index. It is important to point out that α will change with temperature. Accordingly, the thermal properties of graphite are treated as functions of temperature (see Section II. D) and allowed to change in time, but this behavior is approximated by using the solution of the temperature profile from the previous time step – denoted by superscript j in Eq. (11). This approach to simplifying the heat equation is acceptable so long as the nozzle is initially at a uniform temperature, which means that the value of α is a known constant at every location within the nozzle, and the subsequent changes in α between time steps are sufficiently small.

A mesh is created to discretize the radial position from the nozzle centreline outward, as shown in Fig. 2. The temperature distribution history within the nozzle is solved for according to Eq. (12), with the nozzle throat wall temperature, T_w, and the nozzle thermocouple measurement temperature, T_{n2}, set as the boundary conditions (see term on the far right of Eq. (12)):

$$\begin{bmatrix} T_{w+\Delta r}^{j+1} \\ T_{w+2\Delta r}^{j+1} \\ \vdots \\ T_{r_{n2}-2\Delta r}^{j+1} \\ T_{r_{n2}-\Delta r}^{j+1} \end{bmatrix} = \begin{bmatrix} b_{w+\Delta r}^{j} & c_{w+\Delta r}^{j} & 0 & 0 & 0 \\ a_{w+2\Delta r}^{j} & b_{w+2\Delta r}^{j} & c_{w+2\Delta r}^{j} & 0 & 0 \\ 0 & \ddots & \ddots & \ddots & 0 \\ 0 & 0 & a_{r_{n2}-2\Delta r}^{j} & b_{r_{n2}-2\Delta r}^{j} & c_{r_{n2}-2\Delta r}^{j} \\ 0 & 0 & 0 & a_{r_{n2}-\Delta r}^{j} & b_{r_{n2}-\Delta r}^{j} \end{bmatrix}^{-1} \left(- \begin{bmatrix} d_{w+\Delta r}^{j} T_{w+\Delta r}^{j} \\ d_{w+2\Delta r}^{j} T_{w+2\Delta r}^{j} \\ \vdots \\ d_{r_{n2}-2\Delta r}^{j} T_{r_{n2}-2\Delta r}^{j} \\ d_{r_{n2}-\Delta r}^{j} T_{r_{n2}-\Delta r}^{j} \end{bmatrix} - \begin{bmatrix} a_{w+\Delta r}^{j} T_{w}^{j} \\ 0 \\ \vdots \\ 0 \\ c_{r_{n2}-\Delta r}^{j} T_{n2}^{j} \end{bmatrix} \right) \tag{12}$$

T_w at $j+1$ Stiffness Matrix T_w at j Boundary

The mesh spacing is kept constant for a firing test, but the number of nodes is shortened to account for the regressing nozzle wall surface. A mesh size of $\Delta r = 10^{-5}$ m and a time sampling interval of $\Delta t = 0.5$ s were used in these calculations. The initial condition applied to Eq. (12) is that the nozzle temperature is at the intial measurement temperature $T_{n2}(t=0)$ at all radial positions, which is acceptable given that combustion, and thus nozzle heating, is just starting to take place at this time.

D. Experimental Apparatus

Two types of static firing test series were necessary for this study: 1) tests where combustion time is the independent parameter, allowing for the NTRT$^+$ to be used and the assumptions of the NTRT to be validated; and 2) tests where oxidizer mass flow rate was the independent parameter, for which only the NTRT can be used. The first type was aimed at confirming the repeatability of tests, and validating the assumptions of constant c^* efficiency in the NTRT and 1D radial conduction in the TTRT, while also collecting data on erosion rate. The second type was dedicated to revealing the conditions at the onset of erosion, as well as determining the constants of the erosion rate formula, Eq. (5).

These tests were carried out on two scales of motors: 30N-thrust class motors, and 2kN-thrust class motors. Depictions of the test setups, nozzle assemblies and screen captures representative of the 30N-thrust class and 2kN-thrust class firing tests are shown in Figs. 3 and 4, respectively. In the 30N-thrust class tests, gaseous oxidizer was

supplied from a single tank, and flow was controlled by a solenoid valve and air actuator. Oxidizer mass flow rate was determined by using a small orifice plate to choke the flow, and measuring the upstream pressure of the orifice according to Eq (13):

$$\dot{m}_{ox} = 0.00248 c_d A_{or} P \quad \text{for gaseous oxygen at 293 K} \tag{13}$$

Where c_d is a dimensionless orifice discharge coefficient determined experimentally, A_{or} is the orifice cross-sectional area in m^2, and P is the orifice upstream pressure in Pa. In the 2kN-class tests, cryogenic (80-90 K) liquid oxidizer was supplied by pressurizing a storage tank with He gas. Oxidizer mass flow rate was determined by measuring the pressure drop across an orifice plate according to Eq. (14):

$$\dot{m}_{ox} = c_d A_{or} \sqrt{2\rho\Delta P} = c_d A_{or} \sqrt{2\left(1630.7 - 5.445T\right)\Delta P} \tag{14}$$

Here the temperature dependency of oxidizer density ρ is based on values from the National Institute of Standards and Technology (NIST) Chemistry Webbook (liquid) [18]. The liquid oxidizer orifice coefficients were determined using water as a working fluid, so there is some uncertainty that is inherently overlooked when applying these constants to determine the flowrate of liquid oxygen. Oxidizer was allowed to fill the piping running between the oxidizer storage tank and the motor injector prior to ignition to ensure that the feed system was pre-cooled. This procedure helped reduce uncertainties in oxidizer mass flow rate due to 2-phase flow at the orifice measurement point. In all tests, ignition was achieved by sending an electrical current through a coil of nichrome wire affixed to the lip of the first fuel block using 1 g of an epoxy/gunpower mixture for 30N-class tests and 5 g of an epoxy/gunpowder mixture for 2kN-class tests (just downstream from the injector). The epoxy/gunpowder mixture was 80% epoxy and 20% gunpowder by weight. Electrical leads from the nichrome coil were fed through the nozzle exit and attached to a DC voltage source. A test section of wire and nichrome coil was attached in series to the main ignition line to allow for a visual confirmation that the current was large enough to heat the nichrome wire. Nichrome wire was heated for 10 s before actuating the oxidizer supply valve and initiating the firing test. Upon completing each firing test, the chamber was purged with gaseous nitrogen, both to extinguish the combustion of fuel and to cool the nozzle.

All tests were conducted using high-density polyethylene (HDPE | formula: C_2H_4) as the fuel, where all 2kN-thrust class tests used a Cascaded Multistage Impinging-jet (CAMUI) type fuel grain, and all 30N-thrust class tests used a conventional tubular fuel grain. Since the shape of fuel at the entrance of the nozzles was similar in all tests, a detailed discussion of fuel design considerations will not be made in this paper. A simplified schematic of these motors is shown in Fig. 5. After assembly, fuel grains were loaded into glass fiber-reinforced plastic (GFRP) insulating tubes and sealed in a steel motor case. The nozzles used in all tests were manufactured using the same grade of isotropic graphite, Tokyo Tokai Carbon Ltd. G347. The density and thermal conductivity at atmospheric conditions are listed by the manufacturer to be ρ_n = 1850 kg/m^3 and k = 116 W/m-K, respectively [19]. The temperature dependency of these and other properties of G347 graphite are not specified by the manufacturer, so values were referenced from previous research on similar high-density graphite. An empirical correlation of data for thermal conductivity based on Fig. 1 in Ref. [20] yields $k(T) = 3712T^{-0.6}$ W/m-K for 200 K < T < 2500 K. An empirical correlation of data for specific heat based on Fig. 1 in Ref. [21] yields $c_p(T) = 651\ln(T)-2877$ J/kg-K for 200 K < T < 3000 K.

E. Data Acquisition and Processing

As required for the data reduction methods, multiple dynamic and static measurements were taken during the experiments conducted in this study. Pressures were measured using KYOWA DCS-10 MPa and KYOWA DCS-5 MPa pressure sensors with rated accuracies of ±0.040 MPa and ±0.028 MPa, respectively. In 30N-thrust class tests thrust was measured using a KYOWA LMB-A-200N load cell with a rated accuracy of ±3.5 N, and in 2kN-thrust class tests thrust was measured using a KYOWA LCTA-A load cell with a rated accuracy of ±16 N. Nozzle temperatures were measured using RC Pro k-type thermocouples rated to a maximum temperature of 1100 °C with a response time of 0.3 s. Compression fittings with tapered threading were used to mount the thermocouples to the motor case. These thermocouples had a stiff and electrically insulated metallic lead rod which made it easy to feed the thermocouple through the compression fitting and into the mounting hole. No adhesives were used to fix the thermocouple to the nozzle inner wall, but the compression fittings were tightened to ensure contact. As suggested by Sutton in Ref. [22] (p. 459), the burn time t_b of a firing test is taken to be the duration between when the chamber (gauge) pressure reaches 10% of the maximum value and the aft-tangent bi-sector at shutdown. These criteria were also used in Ref. [9] and [10].

Initial and final nozzle throat diameter measurements in the 30N-class nozzles were taken by analyzing digital photographs of the nozzle before and after firing using ImageJ [23]. These photographs were taken at 40x digital zoom

from a distance of two meters from the nozzle throat. A length scale was established for the scan by placing a plaque of 1 mm spacing grid paper next to the nozzle being scanned. This procedure was repeated five times before and after each firing test and the standard deviation of these measurements was incorporated into the uncertainty of this measurement, however the standard deviation of measurements was typically much smaller than the uncertainty of the length scale. The length scale uncertainty was assumed to be two times the thickness of a grid line (0.2 mm). Initial and final nozzle throat diameter measurements in the 2kN-class nozzles were taken using a Mitutoyo NTD14-20PMX digital caliper. These measurements were repeated a minimum of 12 times, at angles of 0, 45, 90 and 135 deg with respect to the chamber pressure port inlet.

F. Uncertainty Analysis

Uncertainty in the experimental measurements of thrust, pressure etc. propagate through the data reduction, the intermediary property calculations and ultimately to the results of data reduction. The details of this process are summarized in Refs. [9] and [10]. For example, applying this principle to determine the uncertainty in the results for the Schmidt number of Eq. (4) results in Eq. (15):

$$U_{\mathrm{Sc_{CO}}} = \sqrt{\left(\frac{\partial \mathrm{Sc_{CO}}}{\partial D_{\mathrm{CO},w}} U_{D_{\mathrm{CO},w}}\right)^2 + \left(\frac{\partial \mathrm{Sc_{CO}}}{\partial \mu} U_{\mu}\right)^2} \tag{15}$$

Here, U is the uncertainty of the term in the subscript. Note that neither of the terms in Eq. (15) are direct measurements. Each of these terms' uncertainties is the accumulation of the uncertainty in one or more of the direct measurements. The computer program developed to run data reduction calculations carefully tracks these uncertainties through the tiers of operation – starting with direct measurement values and propagating through the NTRT, NASA CEA operations, etc.

III. Results and Discussion

In total, 44 static firing tests were conducted for this study: 32 x 30N-thrust class tests and 12 x 2kN-thrust class tests. The pertinent results of these firing tests are listed in Table 1. These tests were conducted over the course of more than three years from 2015 to 2018. The tests have been listed by their local series name to represent how many groupings of tests that there were, but this does not necessarily reflect the chronology of experimentation. Roughly

speaking, ERM series tests were conducted first, followed by the HK series, DNT series, SLY series, MSS series and QE series.

The data reduction terms of MSS-2 thru -7 have been plotted in Figs. 6-8 for two reasons. First, these tests well represent the capability of the data reduction techniques and progression of nozzle erosion that can lead to performance loss in a hybrid rocket. Second, a large substitution is being made for MSS-2 thru -6, which these figures help clarify. The test with the longest combustion time, MSS-7, was the first MSS series test in which thermocouple measurements were taken, nozzle temperature measurements were not taken in MSS-2 thru -6. However, all tests MSS-2 thru MSS-7 were conducted using the same initial conditions and motor design, for which only the time at shutdown was varied between tests. Around 15 s into MSS-7 (of a 25 s test) the injector begun to burn through, resulting in very large oscillations in pressure and flowrate. Due to the very high repeatability of chamber pressure and oxidizer mass flow rate in MSS-2 thru -7 up to 10 s (see Figs. 6(b)-8(b)), the thermocouple measurements of MSS-7 were used for the empirical correlation of MSS-2 thru -6. As can be seen from Fig. 9, which plots all relavent temperature histories of MSS-7, the thermocouple T_{n1} fails around 15 s into the firing due to overheating, whereas the thermocouples T_{check} and T_{n2} survive the whole firing duration.

A. Repeatability of Results and Validation of the NTRT and TTRT

In the DNT-15 thru -18 tests, the flow rate was set to a very low value of 8.1-8.2 g/s, and tests were repeated with burn times of 5 s, 10 s, 15 s, and 20 s. The result was an amount of nozzle throat erosion that was barely measurable, < 0.01 mm/s on average, however the measurement inputs to the NTRT were satisfactorily repeatable, and the resulting η^* was constant in tests longer than 5 s. In the 5 s test, the start-up transient likely had the effect of lowering the apparent η^*, and this was probably compounded by the very low oxidizer flow rate. In the second set, tests DNT-3 thru -6, the flow rate was a value of 11.3-11.4 g/s. The results show that even for the 5 s test η^* showed little dependency on the combustion time. In the third set, tests MSS-2 thru -6, the results are similar to those of the 30N-class tests, but with efficiencies slightly larger than 100%. This is an attribute of the Cascaded Multistage Impinging-jet (CAMUI) type fuel design which by nature has excellent mixing and enhanced heat transfer to the fuel. The recovery of dynamic pressure from the flow in the pressure port, as well as uncertainty in the measurement of liquid oxygen mass flow rate using an orifice plate are probable explanations for why the efficiency appears to exceed 100%.

The above tests were also used to confirm the validity of the TTRT results for nozzle throat wall temperature, however this did not require the special procedure of repeating tests at various combustion times. The TTRT results

were considered validated if the resulting temperature profile histories agreed with the experimental value of a third, unused, "check" thermocouple measurement. An example of this confirmation method is depicted in Fig. 10 where the check thermocouple temperature is shown by red diamonds. Figure 10 shows that the results of TTRT for test MSS-7 as substituted to MSS-5, which had substantial nozzle erosion, agree well with the experimental value of the check thermocouple.

The validity of the assumption that heat transfer is 1D in the radial direction is examined using Fig. 11. Here, Bartz's correlation from Ref. [24] is applied to estimate the convective heat transfer coefficient h [W/m^2-s] (listed as "convectivity" for brevity) from the nozzle inlet to the nozzle exit of a 30N-thrust class nozzle profile. The value of h is roughly 15 times larger at the throat (r = 2 mm) than at the entrance (r = 7 mm). Thus, the value of h corresponding to the location of T_{n2} (r = 12 mm) is expected to be even less than 1/15 of the value at the throat. With the good agreement of the check thermocouple measurements in most cases in which they were available, and a general trend for convective heat flux to decrease sharply near the nozzle entrance, the uncertainty of the approximation of 1D heat transfer was deemed to be low enough to move forward with erosion rate analysis.

B. Empirical Formula for Nozzle Erosion Rate

Erosion rates were taken as linear approximations of the slope of the nozzle throat radius histories determined at a sampling rate of 2 Hz. Similarly, averages were taken at 0.5 s intervals for all correlation data corresponding to the nozzle erosion rates. Due to large oscillations in the initial one to two seconds during startup of a firing test, nozzle erosion rate was assumed to be zero until the moment of a conspicuous and continuous increase in nozzle throat radius in time. This resulted in a set of data consisted of 848 data points, including the data just after startup where nozzle erosion is taken to be zero. The constants of Eq. (5) were determined using the least squares method where the initial guesses for each constant were: $\beta_1 = \beta_2 = \beta_3 = 1$; b=0; E=2000; and n = 0.5. The resulting formula is listed as Eq. (16):

$$\frac{d\dot{r}}{D_{CO,w}} = (0.002)\Phi^{5.43}\exp(-6.36\Phi)T_w^{-0.02}\exp\left(-\frac{6436}{T_w}\right)P^{1.02}\left(\frac{\rho_w}{\rho_n}\right)\mathrm{Re}^{0.83}\,\mathrm{Sc}_{\mathrm{CO}}^{0.44} \tag{16}$$

where d is the throat diameter in m, $D_{CO,w}$ is in m^2/s, $\dot{r}$ is in m/s, T_w is in K, P is in Pa, ρ_n and ρ_w are in kg/m^3, and Φ, Re and $\mathrm{Sc}_{\mathrm{CO}}$ are dimensionless. Note that in Eq. (16), $D_{CO,w}$ is the binary diffusion coefficient of CO and Air at the nozzle wall temperature and the exponents of Re and $\mathrm{Sc}_{\mathrm{CO}}$ were referenced from previous literature (see Section II-

A). Even given the large amount of data collected through the use of the data reduction methods, the correlation of determination of Eq. (16) is very poor, as shown in Fig. 12 to be a meager R2 = 0.33. However, it was clear through the inspection of nozzle erosion histories that at a sampling rate of 2 Hz the erosion rate oscillates in time due to the discretization. This means that much scatter can be cleared up by integrating in time to track the overall erosion. Unfortunately, in many of the tests, the thermocouples fail due to overheating partway through the test. In these cases, the last known value of T_w was taken to be the wall temperature for all times after which thermocouple failure occurred due to overheating so that Eq. (16) could be integrated for the entire burn time. The results of analysis of overall erosion rate are shown in Fig. 13. The correlation of determination doubles to R2 = 0.65, demonstrating that the discretization of erosion histories led to much of the scatter. The remaining disagreement between measured and calculated values of overall erosion may be the result of a number of causes. Two causes that seem likely are the non-circular erosion of the throat, which leads to variations in the thermocouple depths that cannot be tracked using the data reduction techniques, and the fact that T_w values are being assumed for large portions of integration for cases in which thermocouples fail due to overheating.

C. Onset of Nozzle Erosion

In a pure mathematical interpretation of the Arrhenius equation, nozzle throat erosion is always happening with some probability. However, in practice, nozzle throat erosion is not measurable until noticeable changes in the nozzle throat area take place. Since oxidizer-to-fuel-mass ratios were decreasing in the beginning of the tests, and oxidizer mass flow rates and chamber pressures reached quasi-steady-state values before nozzle erosion occurred, the only explanation based on Eq. (5) for the time-dependent behavior of the onset of erosion observed in Fig. 8 is the exponential temperature dependency. A new term, defined as the "Erosion Onset Factor" was conceived of to investigate the chemical-kinetic threshold of nozzle erosion. This term was given the Greek alphabet Π and formulated according to Eq. (17):

$$\Pi_{on} = \exp\left(-E_{on}/T_{w,on}\right) P_{on}^{n_{on}} = A\exp\left(B\Phi_{on}\right) \tag{17}$$

Here, the subscript "*on*" indicates that the value is that at the time of the "onset" of erosion, i.e. t_{on}. The pressure P_{on} is the pressure at the throat, and the terms A and B are constants of correlation. In the correlation of Π_{on}, all possible

sets of $0 < E_{on} < 10000$ (10 K intervals) and $0 < n_{on} < 2$ (0.01 intervals) are tested against the correlation of *A* and *B*. The set that leads to the highest coefficient of determination is chosen to be the solution. This result is shown in Fig. 14, which plots the values of Π_{on} versus the equivalence ratio at that time Φ_{on}. The time at the onset of erosion was defined to be that before which nozzle throat erosion rate is equal to or larger than 0.01 mm/s for at least 1 s, which was considered to be the limitation of the accuracy of the results of the data reduction technique. Of the 44 tests, 40 had identifiable erosion onset times, resulting in an erosion onset factor correlation with R2 = 0.71.

A few interpretations of the Π_{on} correlation will be discussed here. First, this correlation is unrelated to the flow geometry and therefore scale of the flow field. This agrees with the preconception that the onset of erosion is chemical kinetic-limited. The strong correlation between Π and Φ at the onset of erosion also reinforces this conclusion. In general, it is to be expected that erosion takes place more freely in oxidizer rich conditions than in fuel rich conditions. It is in this discussion that the form of the curve fit used for the empirical correlation of Eq. (17) was selected. Second, the authors recognized that even in a pure oxidizer – representative of very small values for Φ – at room temperature and pressure, nozzle erosion will not take place. This means that Π_{on} has a positive non-zero y-intercept. In very fuel rich conditions, there are essentially no oxidizing agents in the combustion gas, thus erosion cannot be expected to take place even at high temperatures and pressures. In following, the authors selected an exponential function for the curve fit of Π as shown in Fig. 14, which shows that in oxidizer rich conditions ($\Phi < 1$) erosion begins at lower temperatures and pressures than in fuel-rich conditions ($\Phi > 1$), that there is a positive threshold for erosion at $\Phi = 0$, and that the threshold for erosion in very fuel rich conditions ($\Phi >> 1$) tends to infinity. In this way, the inequality shown in Eq. (18) can be treated as a threshold for the onset of nozzle erosion:

$$\textit{if} \quad \exp\left(-2430/T_w\right)P^{1.32} > \left(3.17\times10^{6}\right)\exp\left(1.32\Phi\right) \quad \textit{then} \ \text{erosion region} \tag{18}$$

If the temperature and pressure are high enough for the corresponding equivalence ratio, erosion will occur. In most cases, the onset of erosion can be explained by the transient heating of the nozzle since the pressure and equivalence ratio usually reach their steady state values before erosion begins to occur. However, according to this interpretation, there are a number of seemingly unrelated operations that may lead to or prevent nozzle erosion, such as: a throttling maneuver which changes the chamber pressure; or a severe ξ-shift during firing due to the change in fuel burning surface area etc.

IV. Conclusion

As hybrid rockets continue to increase in scale and performance, and capture the attention of the commercial sector as a safe and low-cost propulsion system, the issue of nozzle erosion will become more relevant. Until recently, there have been no detailed reports on the nozzle erosion characteristics specific to hybrid rockets. This study is one of the first of its kind offering an experimental investigation of graphite nozzle throat erosion in two scales of hybrid rockets – 30N-thrust class and 2000N-thrust class – using oxygen as the oxidizer and high-density polyethylene as the fuel. One particularly unique aspect of this research is that it employs a newly introduced data reduction method to estimate nozzle throat erosion histories and oxidizer-to-fuel-mass ratio history, and proposes a follow-on technique to quantify the wall temperature at the nozzle throat. Through the combination of these techniques, over 800 data points of nozzle throat erosion rate were collected from just 44 static firing tests. These data enabled the development of an empirical model that treats the combustion gas passing through the nozzle as a bulk oxidizing agent, rather than as separate oxidizing species. In this way the heterogeneous chemical reaction rate coefficient of the combustion gas could be represented as a distribution of equivalence ratio. The resulting correlation satisfactorily ($R2 > 0.6$) reproduces the overall nozzle throat erosion of the tests conducted by the authors. Furthermore, this report was able to clarify the chemical-kinetic limiting conditions of the onset of nozzle erosion through a novel empirical term referred to as erosion onset factor.

Acknowledgments

This research is supported by the Ministry of Education, Science, Sports and Culture, Grand-in-Aid for Science Research (B). 15H04197, 2016, Grant-in-Aid for JSPS Fellows 18J2087708, and by a matching fund program of Centers for Inter-University Collaboration from ISAS (Institute of Space and Astronautical Science), JAXA (Japan Aerospace Exploration Agency).

References

[1] Delaney, L., Eagleton, L., Jones, W., "A Semiquantitative Prediction of the Erosion of Graphite Nozzle Inserts," *AIAA Journal*, Vol. 2, No. 8, 1964, pp. 1428–1433.
doi: 10.2514/3.2570

[2] McDonald, A., Hedman, P., "Erosion of Graphite in Solid-Propellant Combust Gases and Effects on Heat Transfer," *AIAA Journal*, Vol. 3, No. 7, 1965, pp. 1250-1257.

doi: 10.2514/3.3117

[3] Mayberry, J., Kordig, J., Zeamer, R., Browning, S., "Correlation of Graphite Nozzle Throat Erosion in Solid-Rocket Motors.," *AIAA Journal*, Vol. 6, No. 11, 1968, pp. 2222–2224.
doi: 10.2514/3.4972

[4] Keswani, S., Andiroglu, E., Campbell, J., Kuo, K, "Recession Behavior of Graphite Nozzles in Simulated Rocket Motors," *Journal of Spacecraft and Rockets*, Vol. 22, No. 4, 1985, pp. 396-397.
doi: 10.2514/3.25763

[5] Whitmore, S., Peterson, Z., Eilers, S., "Closed-Loop Precision Throttling of a Hybrid Rocket Motor," *Journal of Propulsion and Power*, Vol. 30, No. 2, 2014, pp. 325-336.
doi: 10.2514/1.B34924

[6] Jens, E., Karp, A., Rabinovitch, J., Nakazono, B., Conte, A., Vaughan, D., "Design of Interplanetary Hybrid CubeSat and SmallSat Propulsion Systems," *54th AIAA/ASME/SAE/ASEE Joint Propulsion Conference*, AIAA Paper 2018-4668, July 2018.
doi: 10.2514/6.2018-4668

[7] Yuasa, S., Kitagawa, K., Sakurazawa, T., Kumazawa, I., Sakurai, T., "Liquid Oxygen Vaporization Techniques for Swirling-Oxidizer-Flow-Type Hybrid Rocket Engines," *International Journal of Energetic Materials and Chemical Propulsion*, Vol. 10, No. 2, 2011, pp. 155–168.
doi: 10.1615/IntJEnergeticMaterialsChemProp.2012001351

[8] Saito, Y., Yokoi, T., Yasukochi, H., Soeda, K., Totani, T., Wakita, M., Nagata, H., "Fuel Regression Characteristics of a Novel Axial-Injection End-Burning Hybrid Rocket," *Journal of Propulsion and Power*, Vol. 34, No. 1, 2018, pp. 247-259.
doi: 10.2514/1.B36369

[9] Kamps, L., Saito, Y., Kawabata, R., Wakita, M., Totani, T., Takahashi, Y., Nagata, H., "Method for Determining Nozzle-Throat-Erosion-History in Hybrid Rockets," *Journal of Propulsion and Power*, Vol. 33, No. 6, 2017, pp. 1369-1377.
doi: 10.2514/1.B36390

[10] Kamps, L., Sakurai, K., Saito, Y., Nagata, H., "Comprehensive Data Reduction for N2O/HDPE Hybrid Rocket Motor Performance Evaluation," *Aerospace*, Vol. 6, No. 45, pp. 1-22, 2019.
doi: 10.3390/aerospace6040045

[11] Acharya, R., Kuo, K., "Effect of Pressure and Propellant Composition on Graphite Rocket Nozzle Erosion Rate," *Journal of Propulsion and Power*, Vol. 23, No. 6, 2007, pp. 1242-1254.

doi: 10.2514/1.24011

[12] Thakre, P., Yang, V., “Chemical Erosion of Refractory-Metal Nozzle Inserts in Solid-Propellant Rocket Motors,” *Journal of Propulsion and Power*, Vol. 25, No. 1, 2009, pp. 40-50.
doi: 10.2514/1.37922

[13] Bianchi, D., Nasuti, F., Onofri, M., Martelli, E., “Thermochemical Erosion Analysis for Graphite/Carbon-Carbon Rocket Nozzles,” *Journal of Propulsion and Power*, Vol. 27, No. 1, 2011, pp. 197-205.
doi: 10.2514/1.47754

[14] Gordon, S., McBride, B., “Computer Program for Calculation of Complex Chemical Equilibrium Compositions and Applications,” NASA RP-1311, 1994.

[15] Chelliah, H., “The Influence of Heterogeneous Kinetics and Thermal Radiation on the Oxidation of Graphite Particles,” *Combustion and Flame*, Vol. 104, No. 1–2, 1996, pp. 81–94.
doi: 10.1016/0010-2180(95)00107-7

[16] Turns, S., *An Introduction to Combustion: Concepts and Applications*, 3rd ed., McGraw-Hill, Singapore, pp. 708-709.

[17] Gilliland, E., Sherwood, T., “Diffusion of Vapors into Air Streams,” *Industrial and Engineering Chemistry*, Vol. 26, No. 5, 1934, pp. 516–523.
doi: 10.1021/ie50293a010

[18] “NIST-JANAF Thermochemical Tables,” Accessed Online <https://janaf.nist.gov> , 25th May 2018.

[19] “ISOTROPIC GRAPHITE: Typical properties,” Accessed Online <https://www.tokaicarbon.co.jp/en/products/fine_carbon/pdf/Isotropic_graphite.pdf>, 13th June 2018.

[20] Lutcov, A., Volga, V., Dymov, B., “Thermal Conductivity, Electric Resistivity and Specific Heat of Dense Graphite,” *Carbon*, Vol. 8, 1970, pp. 753-760.
doi: 10.1016/0008-6223(70)90100-4

[21] Butland, A., Maddison, R., “The Specific Heat of Graphite: An Evaluation of Measurements,” *Journal of Nuclear Materials*, Vol. 49, 1973, pp. 49-56.
doi: 10.1016/0022-3115(73)90060-3

[22] Sutton, G., Bibliarz, O., *Rocket Propulsion Elements*, 8th ed., John Wiley & Sons, Inc., 2010.

[23] Rasband, W., “ImageJ,” U.S. National Institutes of Health, Bethesda, MD, 1997.

[24] Bartz, D., “A Simple Equation for Rapid Estimation of Rocket Nozzle Convective Heat Transfer Coefficients,” *Journal of Jet Propulsion*, Vol. 27, No. 1, 1957, pp. 49-53.
doi: 10.2514/8.12572

Table 1 Summary of test results

Test	t_b	d_o	d_f	ΔM_{fu}	$\bar{\dot{m}}_{ox}$	$\bar{P}_c$	$\bar{F}$	$\bar{T}_{n,1}$	$\bar{T}_{n,2}$	$\bar{T}_{n,3}$	$\bar{\eta}^*$
	s	mm	mm	g	g/s	MPa	N	K	K	K	
30N-thrust class firing tests											
DNT-2	20	4.0	6.5	72	12	1.2	26	>1295	1190		0.82
DNT-3	15	4.0	5.0	52	11	1.4	26	>1133	1030		0.79
DNT-4	25	4.0	6.3	79	11	1.0	24	>1352	>1190	1109	0.78
DNT-6	10	4.0	4.4	33	12	1.5	25	970	765	715	0.82
DNT-10	25	4.0	5.9	87	11	1.3	26	>1345	>1184	>1142	0.90
DNT-11	17	4.0	5.3	63	11	1.4	25	>1290	984	907	0.85
DNT-12	15	4.0	4.3	41	9	1.2	20	946		709	0.80
DNT-13	17	4.0	5.3	52	9	1.1	20	>1230	926	896	0.82
DNT-14	12	4.0	4.6	34	8	1.1	19	>1112	804	758	0.81
DNT-15	5	4.0	4.0	12	8	1.0	17	592	555	528	0.72
DNT-16	10	4.0	4.1	26	8	1.2	18	837	754	705	0.77
DNT-17	15	4.0	4.2	41	8	1.1	20	1068	843	798	0.78
DNT-18	20	4.0	4.2	61	8	1.2	21	1071	860	780	0.79
DNT-19	5	4.0	4.4	14	11	1.4	19	751	543	529	0.79
DNT-20	5	4.0	4.1	15	12	1.5	19	716	560	527	0.80
DNT-21	10	4.0	5.1	31	12	1.3	25	1103	775	769	0.81
HK-8	20	4.0	4.9	71	13	1.5	27	1099	1067	981	0.79
HK-9	20	4.0	5.3	70	14	1.4	27	>1207	>1141		0.75
HK-10	20	4.0	4.3	60	11	1.3	20	1090	893	810	0.75
HK-11	20	4.0	5.6	89	14	1.5	29	>1282	1146	1116	0.79
HK-12	20	4.0	5.9	95	14	1.3	33	>1269	>1141	1080	0.68
HK-13	20	4.0	5.3	61	12	0.9	23	>1226	1076	987	0.58
HK-14	20	4.0	5.4	72	13	1.1	27	>1204	>1189	1114	0.62
SLY-1	20	4.0	5.0	70	10	1.2	24	>1259	977	926	0.76
SLY-2	20	4.0	5.1	64	10	1.1	20	1116	941	870	0.81
SLY-3	20	4.0	4.8	41	12	0.9	15	1178	883	817	0.64
SLY-5	20	4.0	5.3	57	12	1.2	22	1171	967	953	0.75
SLY-6	20	4.0	6.6	56	11	1.0	23	>1347	1133	1056	0.85
SLY-7	20	4.0	5.6	59	11	1.1	23	>1200	1116	1060	0.79
QE-3	5	4.0	4.1	14	11	1.4	24	706	584	540	0.78
QE-4	5	4.0	4.1	16	13	1.6	29	756	553	535	0.75
QE-5	5	4.0	5.0	18	15	1.6	34	833	588	578	0.77
2kN-thrust class firing tests											
ERM-3	5	27.0	27.4	999	554	2.1	1556	607	406		0.93
ERM-4	5	27.0	28.3	785	565	2.0	1523	606	525		0.95
ERM-5	5	27.0	28.1	314	628	1.3	924	570	515		0.84
ERM-8	5	23.0	25.3	825	491	2.6	1492	679	540		1.04
ERM-10	10	23.0	24.0	477	310	1.3	721	827	671		1.04
MSS-2$^+$	4	23.6	23.6	1686	523	3.3	1925	502	366	321	1.06
MSS-3$^+$	7	23.6	24.4	2189	502	3.1	1923	673	448	367	1.06
MSS-4$^+$	13	23.6	27.4	3692	506	3.0	1937	929	588	454	1.07
MSS-5$^+$	19	23.6	30.9	4576	513	2.8	1880	1073	702	525	1.09
MSS-6$^+$	12	23.6	26.2	3543	504	3.1	1953	895	570	443	0.97
MSS-8	11	19.8	19.9	2434	324	2.7	1104	647	465	389	1.06
MSS-12	7	33.4	34.9	2450	729	2.2	2481	729	494	386	1.01

*Time-averages are taken for the entire burn time. Greater than symbols, >, mean that data was not available for the entire burn time.

$^+$ The NTRT$^+$ was used instead of the NTRT.

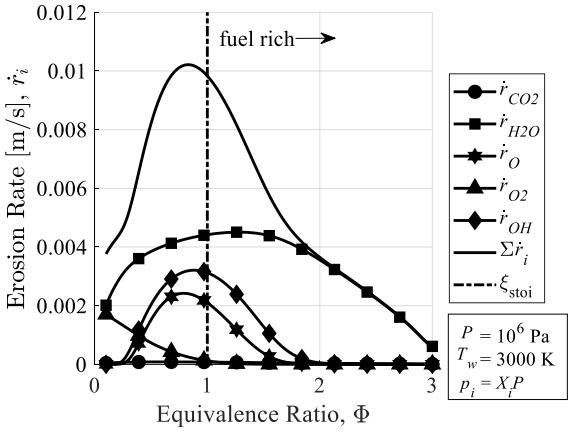

Fig. 1 Erosion rate dependency on equivalence ratio.

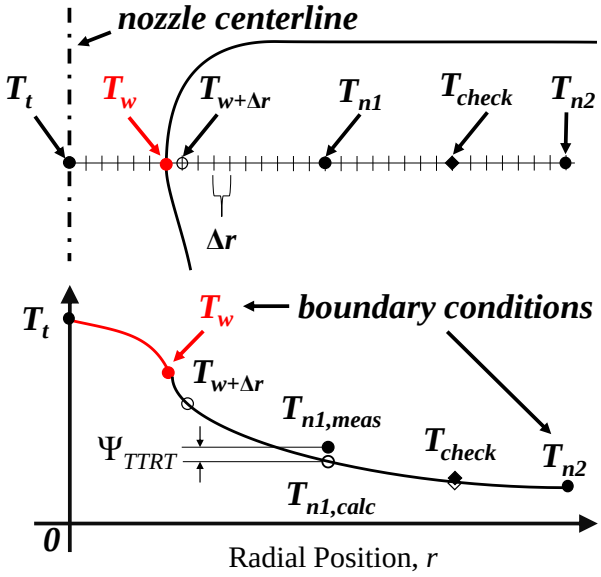

Fig. 2 1D mesh for TTRT calculations. *Terms that require iterative calculations are shown in red.*

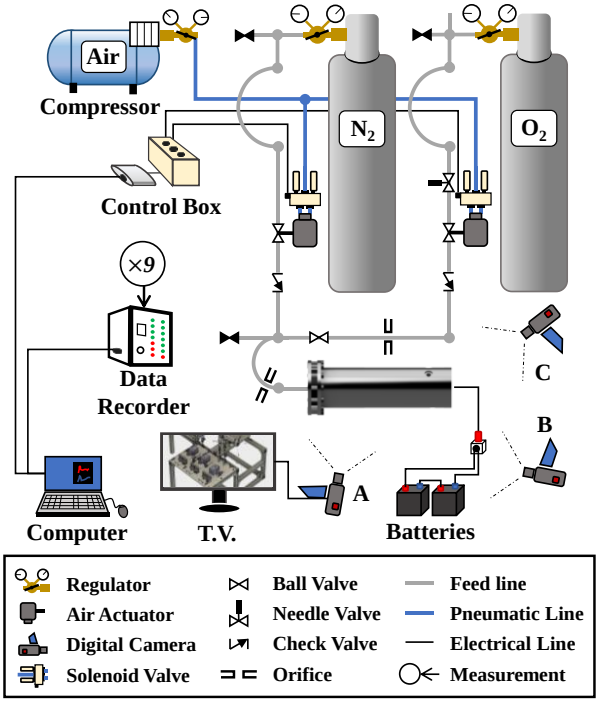

a) Test setup and operation

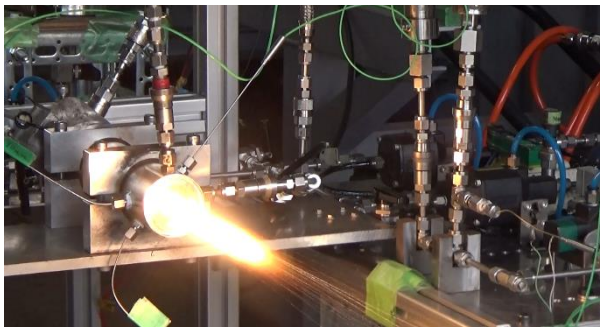

b) Screen capture of firing test QE-5

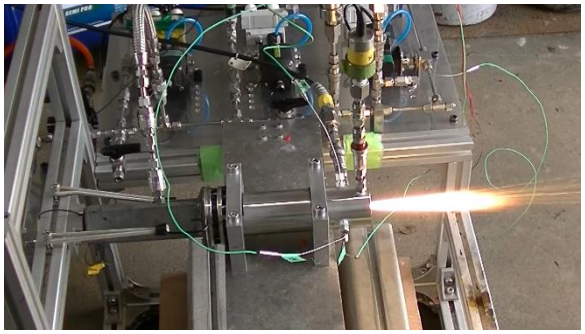

c) Screen capture of firing test DNT-21

Fig. 3 30N-thrust class test apparatus.

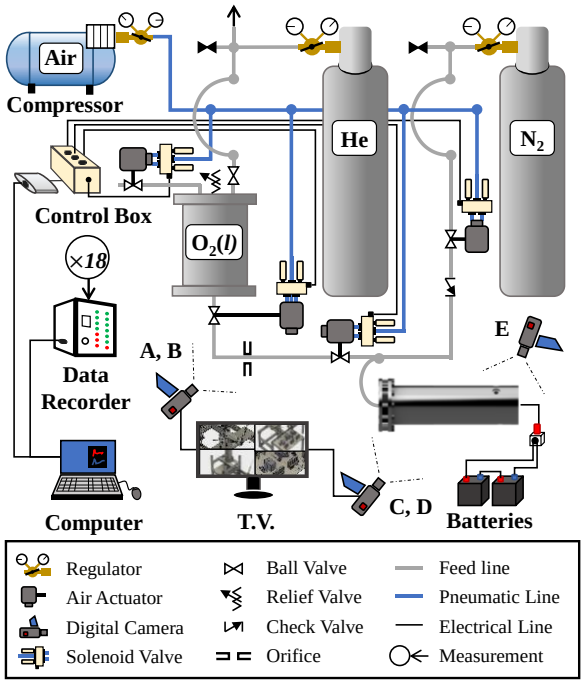

a) Test setup and operation

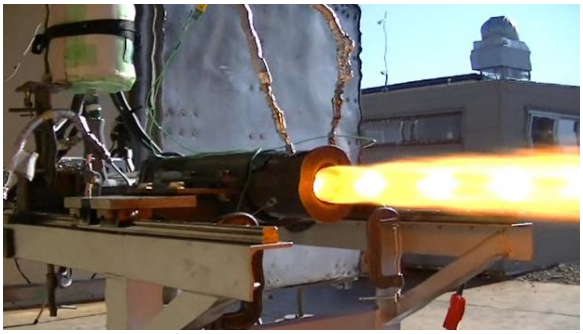

b) Screen capture of firing test ERM-2

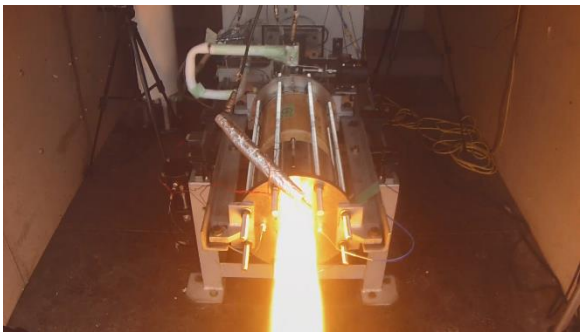

c) Screen capture of firing test MSS-12

Fig. 4 2kN-thrust class test apparatus.

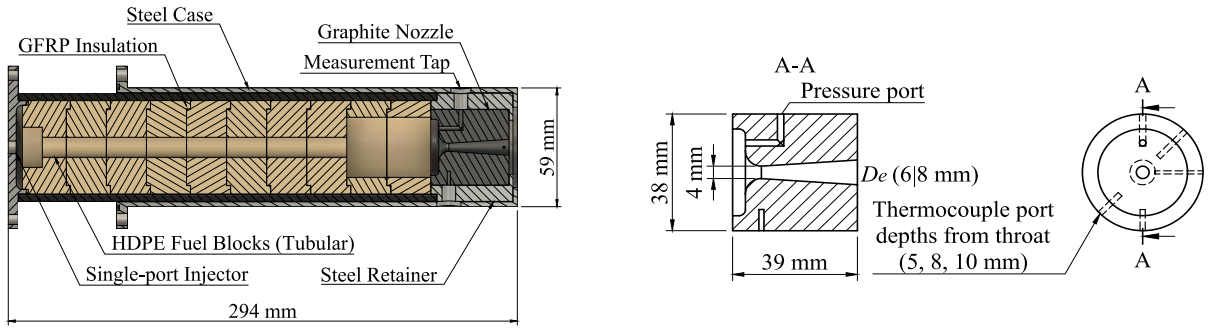

a) Depiction of the motor (left) and nozzle (right) in all 30N tests

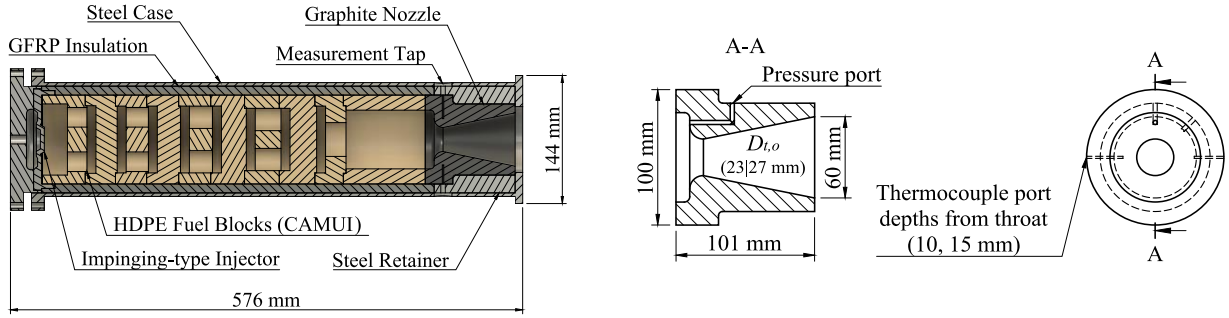

b) Depiction of the motor (left) and nozzle (right) in ERM series tests

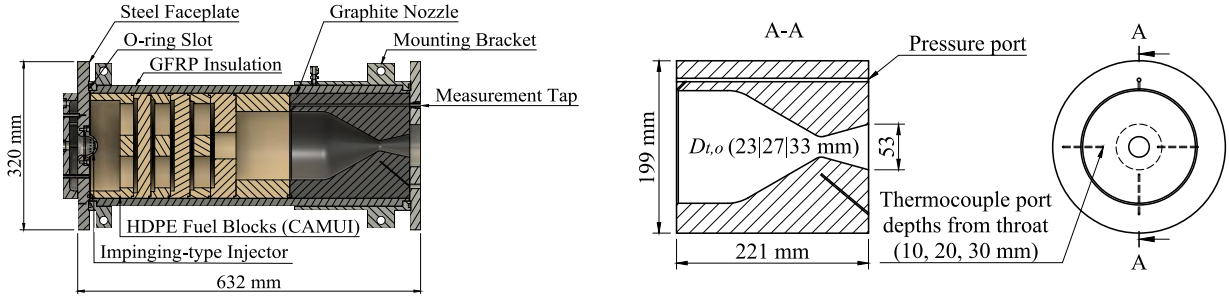

c) Depiction of the motor (left) and nozzle (right) in MSS series tests

Fig. 5 Detailed depictions of the motor assemblies.

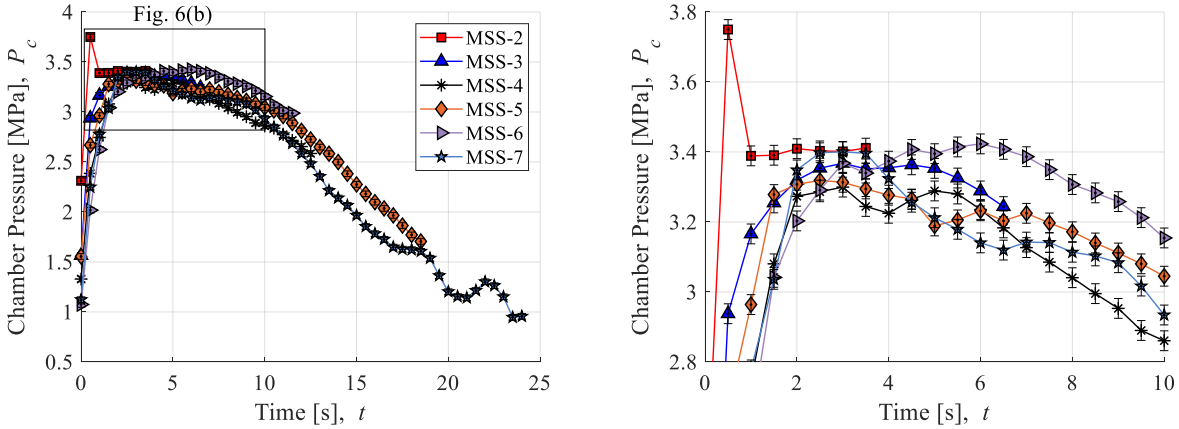

a) Full firing duration **b) Enlarged view of first 10 s**

Fig. 6 Chamber pressure histories of MSS-2 thru MSS-7. *Sampling rate 2 Hz*

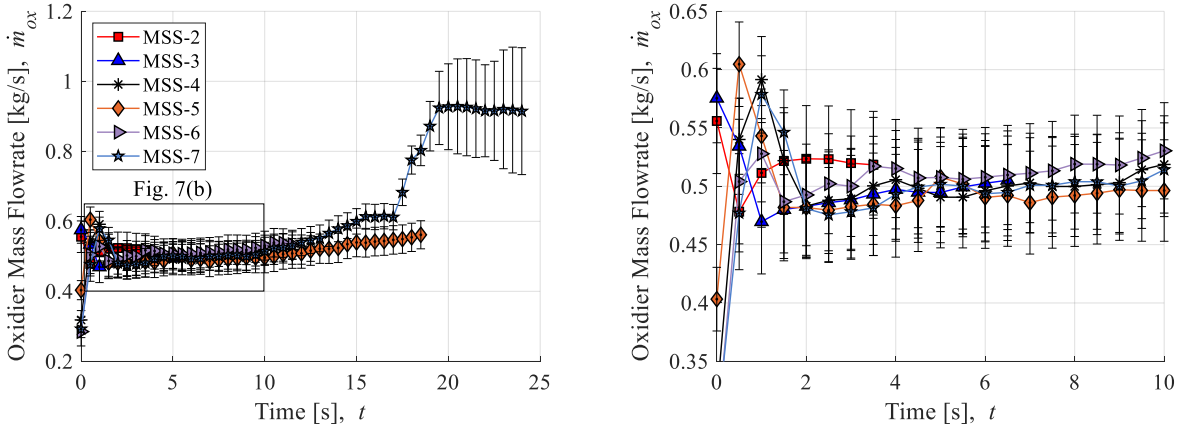

a) Full firing duration **b) Enlarged view of first 10 s**

Fig. 7 Oxidizer mass flow rate histories of MSS-2 thru MSS-7. *Sampling rate 2 Hz*

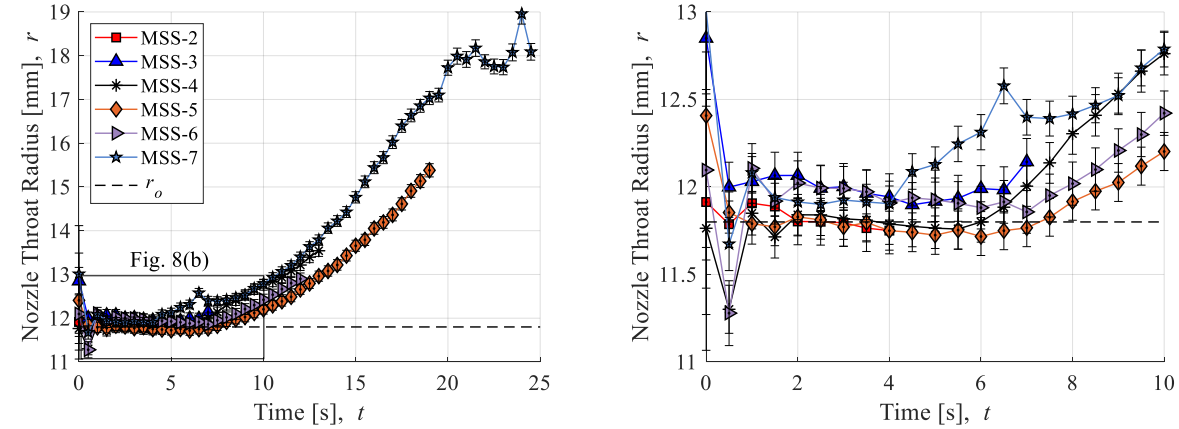

a) Full firing duration **b) Enlarged view of first 10 s**

Fig. 8 Nozzle throat erosion histories of MSS-2 thru MSS-7. *Sampling rate 2 Hz*

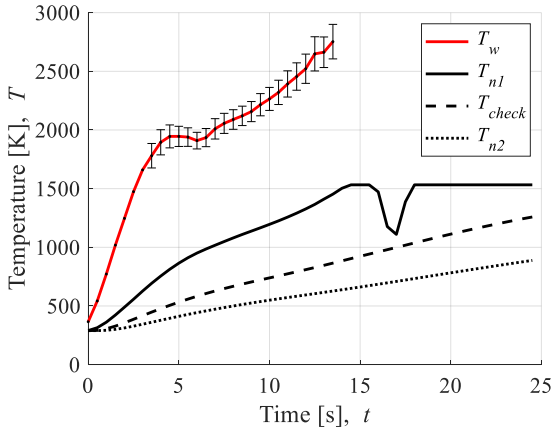

Fig. 9 Nozzle temperature histories of firing test MSS-7.

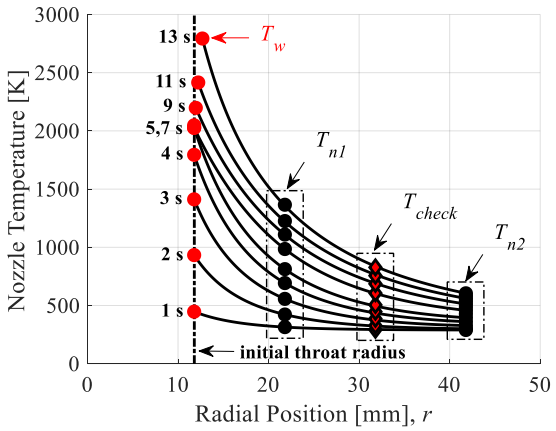

Fig. 10 Example of the validation procedure for TTRT results using a check thermocouple. *Test MSS-5; 31% increase in radius.*

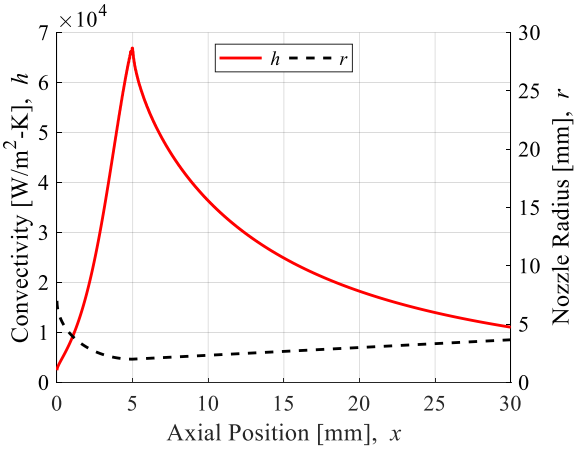

Fig. 11 Heat Transfer is dominant at the throat position. *Nozzle profile from 30N-class schematic.*

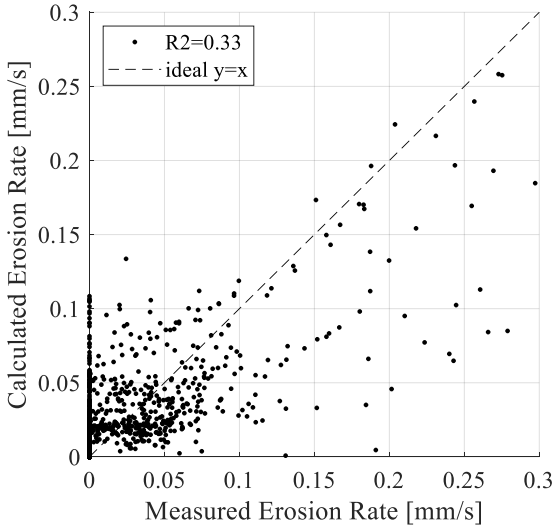

Fig. 12 Large scatter in erosion rate correlation.

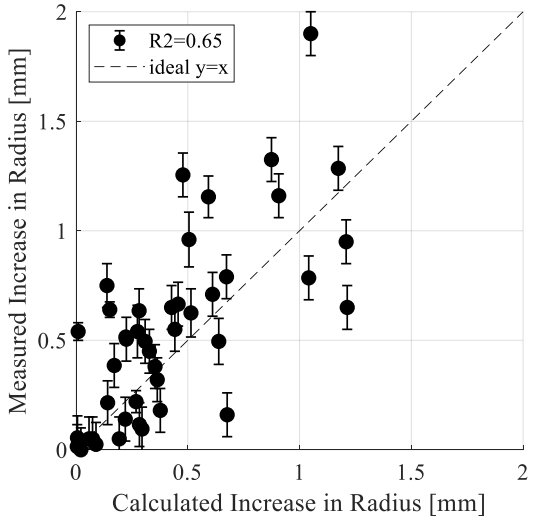

Fig. 13 Smaller scatter in overall erosion correlation.

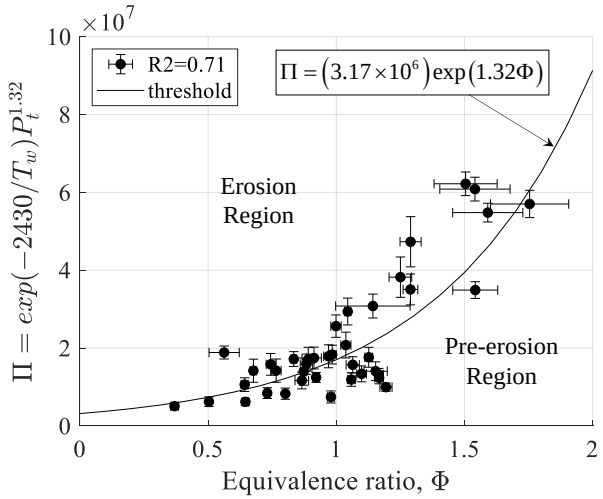

Fig. 14 Empirical correlation of the conditions at the onset of erosion.